



# Validation and application of CPFD models in simulating hydrodynamics and reactions in riser reactor with Geldart A particles



Yingya Wu, Li Peng, Liqing Qin, Min Wang, Jinsen Gao, Xingying Lan \*

State Key Laboratory of Heavy Oil Processing, China University of Petroleum, Beijing 102249, China

## ARTICLE INFO

### Article history:

Received 19 June 2017

Received in revised form 23 September 2017

Accepted 1 October 2017

Available online 9 October 2017

### Keywords:

CFB riser

FCC

CPFD

Geldart A particles

## ABSTRACT

A Computational Particle Fluid Dynamics (CPFD) model, which has the ability of revealing the coupled flow-reaction behaviors on the scales ranging from an individual particle to the whole reactor, was developed for studying the gas-solids circulating fluidized bed (CFB) riser reactor handling Geldart A particles. The model was validated against available experimental data with respects to the hydrodynamics (e.g. distributions of solids holdup and solids velocity) and the reaction behaviors (e.g. distribution of ozone concentration for ozone decomposition), and acceptable agreements were achieved between the modeling results and the experimental data. The CPFD model was further extended for analyzing the gas-solids flow hydrodynamics and the cracking reactions in an industrial Fluid Catalytic Cracking (FCC) riser reactor. Modeling results indicate that the volume of gas in the CFB riser will vary due to the presence of interphase chemical reactions (e.g. catalytic cracking reactions in FCC), which can significantly influence the gas-solids flow hydrodynamics. It was demonstrated that the CPFD model can be applied to quantify the relationship between the flow hydrodynamics and the chemical reactions in multiphase flow-reaction systems.

© 2017 Elsevier B.V. All rights reserved.

## 1. Introduction

Circulating fluidized beds (CFB) with fine Geldart A particles have been widely applied in various industrial processes, e.g. FCC process in refinery, coal combustion, etc. The performance of the CFB is closely related to the complex gas-solids flow hydrodynamics and reaction characteristics inside the CFB riser reactor, which has attracted extensive academic researches through the world [1]. Owing to its advantages of efficiency, convenience and low-cost and its ability in providing more comprehensive and crucial information [2], the Computational Fluid Dynamics (CFD) has gradually become a reliable and effective tool for troubleshooting, designing and scaling-up [3] of the CFB riser through investigating the complex hydrodynamics and reaction characteristics inside the CFB riser.

In most of previous CFD simulations, both Eulerian-Eulerian two-fluid model (TFM) [4] and Eulerian-Lagrangian discrete element model (DEM) [5] have been used for studying gas-solids fluidized beds [6,7]. Despite that the TFM model treating gas and solid phases as two interpenetrating continua can deal with large-scale industrial systems, it cannot accurately consider the realistic characteristics of particles. Due to the pseudo-fluid rheological properties of solid phase especially for fine Geldart A particles [8], the reliability and accuracy of

some of the empirical relations for describing the strong interparticle forces [9,10], including interfacial friction, shear stress, and cohesive force, are still in dispute in the TFM, which is a limitation of the TFM. In contrast, the DEM model can individually track each particle by solving the Newton equation [11,12], which indicates that the detailed particle flow behaviors in fluidized beds can be predicted in DEM [13]. However, the huge computational requirements of DEM in describing dense particle-particle interactions are proportional to the number of particles simulated [13], which makes it difficult for the DEM in describing a large-scale industrial CFB riser with billions of particles [14].

Currently, in order to overcome the limitations of TFM and DEM, the CPFD model, which is based on multi-phase particle in cell (MP-PIC) method and is in Eulerian-Lagrangian scheme, proposed by Snider and his colleagues [15] has been applied to simulate gas-solids fluidized beds through defining the concept of 'parcel of particles'. Each computational parcel contains a number of particles with identical properties such as density, volume, size, shape and velocity. Due to its unique feature, the CPFD method is capable of simulating large commercial CFB risers containing billions of particles by applying millions of computational parcels [6], and it can serve as a candidate to achieve quick and efficient simulation of industrial gas-solids systems.

Chen et al. [6] studied the applicability of the CPFD method for simulating gas-solids flow hydrodynamics in a CFB riser containing Geldart A particles. They indicated that the drag forces calculated by the conventional drag model including Wen-Yu model, Ergun model, Wen-Yu/Ergun model and Turton model in the CPFD method overestimated

\* Corresponding author at: State Key Laboratory of Heavy Oil Processing, China University of Petroleum, No. 18, Fuxue Road, Changping District, Beijing 102249, China.  
E-mail address: [lanxy@cup.edu.cn](mailto:lanxy@cup.edu.cn) (X. Lan).

**Table 1**  
Detailed governing equations in the simulation.

Fluid phase continuity equation

$$\frac{\partial \theta_f \rho_f u_f}{\partial t} + \nabla \cdot (\theta_f \rho_f u_f) = 0 \quad (\text{T1-1})$$

Gas phase momentum equation

$$\frac{\partial (\theta_f \rho_f u_f)}{\partial t} + \nabla \cdot (\theta_f \rho_f u_f u_f) = -\theta_f \nabla p + \theta_f \mu_f \nabla^2 u_f + \theta_f \rho_f g - F \quad (\text{T1-2})$$

Momentum exchange between gas and particle phases

$$F = \iiint V_p \rho_p |D(u_f - u_p) - \frac{1}{\rho_p} \nabla p| dV_p d\rho_p du_p \quad (\text{T1-3})$$

Liouville equation for finding particle positions

$$\frac{\partial f}{\partial t} + \nabla(u_p) + \nabla_{u_p}(fA) = 0 \quad (\text{T1-4})$$

Particle acceleration

$$A = D(u_f - u_p) - \frac{1}{\rho_p} \nabla p + g - \frac{1}{\theta_p \rho_p} \nabla \tau_p \quad (\text{T1-5})$$

Particle normal stress model

$$\tau_p = \frac{P_s \theta_p^2}{\max(|\theta_{cp} - \theta_p|, \epsilon) (1 - \theta_p)} \quad (\text{T1-6})$$

Particle volume fraction in each cell

$$\theta_p = \iiint V_p dV_p d\rho_p du_p \quad (\text{T1-7})$$

Drag model (Gidaspow model)

$$C_d = \frac{24}{Re} \theta_f^{-2.65} \quad (Re < 0.5) \quad (\text{T1-8})$$

$$C_d = \frac{24}{Re} (1 + 0.15 Re^{0.687}) \theta_f^{-2.65} \quad (0.5 \leq Re \leq 1000) \quad (\text{T1-9})$$

$$C_d = 0.44 \theta_f^{-2.65} \quad (Re > 1000) \quad (\text{T1-10})$$

$$D_1 = 0.75 C_d \frac{\rho_f |u_f - u_p|}{\rho_p} \quad (\text{T1-11})$$

$$Re = \frac{\rho_f d_p |u_f - u_p|}{\mu_f} \quad (\text{T1-12})$$

$$D_2 = \frac{1800 \theta_p}{\theta_p Re} + 2 \frac{\rho_f |u_f - u_p|}{\rho_p} \quad (\text{T1-13})$$

$$D = D_1 \quad (\theta_p < 0.75 \theta_{cp}) \quad (\text{T1-14})$$

$$D = \frac{\theta_p - 0.85 \theta_{cp}}{0.85 \theta_{cp} - 0.75 \theta_{cp}} (D_2 - D_1) + D_1 \quad (0.75 \theta_{cp} \leq \theta_p \leq 0.85 \theta_{cp}) \quad (\text{T1-15})$$

$$D = D_2 \quad (\theta_p > 0.85 \theta_{cp}) \quad (\text{T1-16})$$

Drag model (EMMS model)

$$\beta = \frac{3}{4} C_D \frac{\rho_p \rho_f |u_f - u_p|}{d_p} H_D \quad (\text{T1-17})$$

$$C_D = \frac{24(1 + 0.15 Re_p^{0.678})}{d_p} \quad (Re_p < 1000) \quad (\text{T1-18})$$

$$C_D = 0.44 \quad (Re_p \geq 1000) \quad (\text{T1-19})$$

$$Re_p = \frac{\rho_f \rho_f |u_f - u_p| d_p}{\mu_f} \quad (\text{T1-20})$$

$$H_D = a(Re_p + b)^c \quad (\text{T1-21})$$

For the CFB riser under  $G_s = 200 \text{ kg}/(\text{m}^2 \cdot \text{s})$ ,  $U_g = 7 \text{ m/s}$

$$a = \begin{cases} \exp(0.5120 + 471.7406 \epsilon_f^{2.5} + 116.8694 \frac{\epsilon_f}{\ln \epsilon_f}) & 0.457 \leq \epsilon_f < 0.8 \\ \frac{1}{(0.5690 + 11201.4430 \ln^2 \epsilon_f - \frac{0.0001868}{\ln \epsilon_f})} & 0.8 \leq \epsilon_f < 0.9997 \quad (\text{T1-22}) \\ 1 & 0.9997 \leq \epsilon_f < 1 \end{cases}$$

$$b = \begin{cases} \frac{\epsilon_f}{(-0.05570 \exp(-\exp(92.9004 - 209.2822 \epsilon_f))) + 9.4089} & 0.457 \leq \epsilon_f < 0.48 \\ -0.8456 \exp(-\exp(141.1489 - 281.1403 \epsilon_f)) + 0.8560 & 0.48 \leq \epsilon_f < 0.6 \\ -0.001343 \exp(\frac{\ln \epsilon_f + 0.2708 \ln^2}{0.01890}) + 0.06095 & 0.6 \leq \epsilon_f < 0.98 \\ 0.6141 - 0.5982 \exp(-361.6032 \epsilon_f^{1177.6292}) & 0.98 \leq \epsilon_f < 0.9997 \\ \frac{0.5498}{(1 + \exp(23.4547 - 44.0615 \epsilon_f)^{0.7882})} & 0.457 \leq \epsilon_f < 0.622 \end{cases} \quad (\text{T1-23})$$

$$c = \begin{cases} 0.9387 - 0.3931 \epsilon_f^{63.0517} - 0.4291 \exp(\epsilon_f) + \frac{0.6075}{\epsilon_f - 0.9801} & 0.622 \leq \epsilon_f < 0.9997 \quad (\text{T1-24}) \\ 0 & 0.9997 \leq \epsilon_f < 1 \end{cases}$$

For the CFB riser under  $G_s = 300 \text{ kg}/(\text{m}^2 \cdot \text{s})$ ,  $U_g = 7 \text{ m/s}$

$$a = \begin{cases} \exp(-14.5750 + 312.7533 \epsilon_f^2 + \frac{88.8204 \epsilon_f}{\ln \epsilon_f}) & 0.457 \leq \epsilon_f < 0.8 \\ \frac{2.1671}{(1.6348 + (\frac{\epsilon_f - 0.9975}{0.004877})^2)} + 0.01925 & 0.8 \leq \epsilon_f < 0.9997 \quad (\text{T1-25}) \\ 1 & 0.9997 \leq \epsilon_f < 1 \end{cases}$$

$$b = \begin{cases} 335829.8019 - 58503.7150 \epsilon_f^2 - 346197.6827 \frac{\ln \epsilon_f}{\epsilon_f} - \frac{283243.1637}{\epsilon_f^{1.5}} & 0.457 \leq \epsilon_f < 0.48 \\ -0.9062 \exp(-\exp(\frac{\epsilon_f - 0.4937}{-0.003305})) + 0.9105 & 0.48 \leq \epsilon_f < 0.6 \\ -0.05969 \epsilon_f^{44.1159} - 0.01195 \epsilon_f^{-2.006296} + 0.0490 & 0.6 \leq \epsilon_f < 0.98 \\ 0.6151 - 0.6007 \exp(-347.2199 \epsilon_f^{1193.8833}) & 0.98 \leq \epsilon_f < 0.9997 \end{cases} \quad (\text{T1-26})$$

$$c = \begin{cases} \frac{0.5657}{(1 + \exp(\frac{(\epsilon_f - 0.5229)^{2.7843}}{0.02132}))} & 0.457 \leq \epsilon_f < 0.622 \\ \exp(-0.7954 + \frac{0.1090}{\ln \epsilon_f} + \frac{0.1300}{\epsilon_f}) & 0.622 \leq \epsilon_f < 0.9997 \quad (\text{T1-27}) \\ 0 & 0.9997 \leq \epsilon_f < 1 \end{cases}$$

For the industrial FCC riser

$$a = \begin{cases} \exp(6.9292 + 588.5260 \epsilon_f^{2.5} + \frac{154.9300 \epsilon_f}{\ln \epsilon_f}) & 0.4 \leq \epsilon_f < 0.8 \\ \frac{0.01789}{0.01418 + (\frac{\epsilon_f - 0.9975}{0.04471})^2} + 0.01863 & 0.8 \leq \epsilon_f < 0.9997 \quad (\text{T1-28}) \\ 1 & 0.9997 \leq \epsilon_f < 1 \end{cases}$$

$$b = \begin{cases} 731763.7904 - 340361.2073 \epsilon_f - \frac{943439.1025}{\epsilon_f} + \frac{659574.2703}{\epsilon_f^{1.5}} - 135074.8485 \epsilon_f^2 & 0.4 \leq \epsilon_f < 0.46 \\ 1.3451 \exp(-\exp(-37.9801 + 83.8802 \epsilon_f)) + 0.01152 & 0.46 \leq \epsilon_f < 0.53 \\ -27.9991 + 143.2336 \epsilon_f - 270.8919 \epsilon_f^2 + 226.7026 \epsilon_f^3 - 71.04820 \epsilon_f^4 & 0.53 \leq \epsilon_f < 0.95 \\ 0.3866 \epsilon_f^{-460.5608 - 96249.5800 \ln \epsilon_f} - 2.03795 \ln \epsilon_f & 0.95 \leq \epsilon_f < 0.9997 \end{cases} \quad (\text{T1-29})$$

$$c = \begin{cases} \frac{1}{2.8217 \epsilon_f (1 + 33700572.3662 \exp(-31.7864 \epsilon_f))} & 0.4 \leq \epsilon_f < 0.95 \\ 0.06891 + 0.2873 \exp(-8.5327 \epsilon_f^{201.008284}) & 0.95 \leq \epsilon_f < 0.9997 \quad (\text{T1-30}) \\ 0 & 0.9997 \leq \epsilon_f < 1 \end{cases}$$

the actual gas–solids interactions, and that an improved drag model which took into account the intrinsic heterogeneity in the CFB risers would be required for the CPFD simulations to obtain more accurate results. In addition, based on the open source MFIX, Li et al. [16] applied the MP-PIC method, which was combined with the EMMS drag model, to explore the hydrodynamic characteristics in CFB risers with Geldart A particles. They indicated that the MP-PIC with the EMMS drag model can successfully simulate the gas–solids flow of CFB risers and that this method could serve as a candidate to realize real-time simulation of large-scale industrial processes. Karimipour and Pugsley [17] used the MP-PIC method to simulate the gas–solids bubbling fluidized beds with Geldart A particles. They also concluded that the MP-PIC method was promising in predicting the gas–solids behavior in bubbling fluidized beds. Shi et al. [7] applied the CPFD approach to investigate the hydrodynamics and particles backmixing behavior in CFB riser with Geldart B particles. They indicated that the CPFD method was capable of predicting the hydrodynamics and particles backmixing behaviors.

Moreover, Snider and Banerjee [18] presented that the CPFD method can be applied to study the isothermal and catalytic ozone decomposition reaction. They concluded that the implicit solution of the ozone decomposition and explicit calculation of oxygen generation were successfully achieved with the CPFD method. Snider et al. [19] further applied the CPFD method to investigate the three-dimensional complex inter-dependencies of fluidization, thermal, and chemistry behaviors of the coal gasifier with the commercial-sized reactor. They showed that the complexity of physical and chemical processes in the gas–solids reactor can be dealt with the CPFD method. Although the CPFD method is promising and is anticipated to make valuable contributions in analyzing the complex hydrodynamics and chemical reaction characteristics of gas–solids fluidization beds [15], detailed researches on CFB risers with Geldart A particles using this method are still in developing.

In the present study, firstly, the CPFD approach based on EMMS drag model was developed to simulate the gas–solids flow hydrodynamics in the three-dimensional CFB riser with Geldart A particles. Furthermore, to illustrate the ability of the CPFD approach in describing the futures of chemical reactions in the three-dimensional CFB riser with Geldart A particles, the chemical reaction kinetics for describing the ozone decomposition, which is an isothermal and first-order reaction, were further incorporated into the CPFD approach to develop a comprehensive flow–reaction model. To validate this flow–reaction model, the simulation results with respect to the axial and radial profiles of solids holdup and ozone concentration were compared against the experimental data from Wang [20]. Finally, the CPFD approach with the incorporation of a 14-lump kinetic model was applied to investigate the gas–solids flow hydrodynamics and catalytic cracking reaction characteristics of a large-scale industrial FCC riser reactor.

## 2. CPFD model development

### 2.1. Hydrodynamics governing equations

The CPFD method was based on the commercial software Barracuda 17.0. In CPFD scheme, the continuity and momentum equations are applied to describe the fluid phase, and the MP-PIC formulation [15] is applied to describe the particles momentum transfer. The governing equations and drag model used in this study were summarized in Table 1. Drag models including the EMMS-based drag model and the Gidaspow drag model were compared in describing the interphase interactions.

### 2.2. Gas species transport equations

For each gas species, a transport equation was used to describe the gas phase. The total fluid phase properties from the mass fractions,  $Y_{f,i}$ , of the gas species was obtained. Mass is transferred between gas species during the process of chemical reactions. The chemical source terms  $\delta$

$m_{i,\text{chem}}$  in the individual gas species transport equation can represent the mass transfer between gas species, as shown below:

$$\frac{\partial(\theta_f \rho_f Y_{f,i})}{\partial t} + \nabla \cdot (\theta_f \rho_f Y_{f,i} \mathbf{u}_f) = \nabla \cdot (\theta_f D \rho_f \nabla Y_{f,i}) + \delta m_{i,\text{chem}} \quad (1)$$

where  $\theta_f$  is the volume fraction of the fluid phase,  $\rho_f$  is the fluid density,  $\mathbf{u}_f$  is the fluid velocity vector, the coefficient  $D$  is the turbulent mass diffusivity, which is related to the  $\mu$  (viscosity) and is calculated by the  $Sc$  (Schmidt number correlation), as shown below:

$$Sc = \frac{\mu}{\rho_f D} \quad (2)$$

where the standard value of the turbulent  $Sc$  is 0.9.

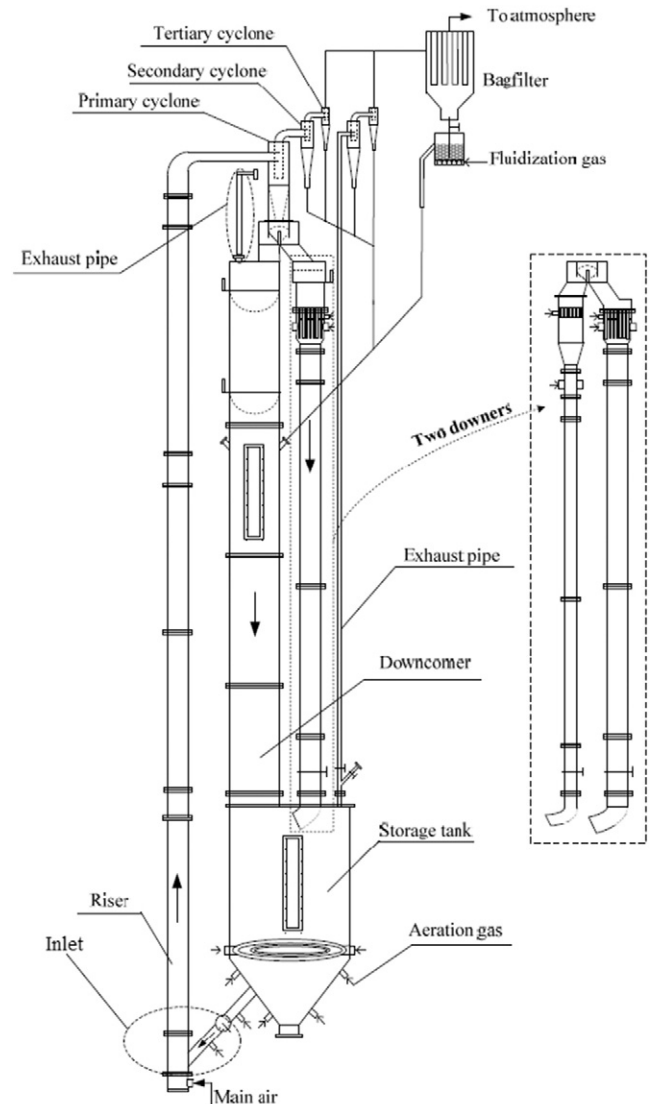


Fig. 1. Schematic diagram of the CFB riser in the experiment.

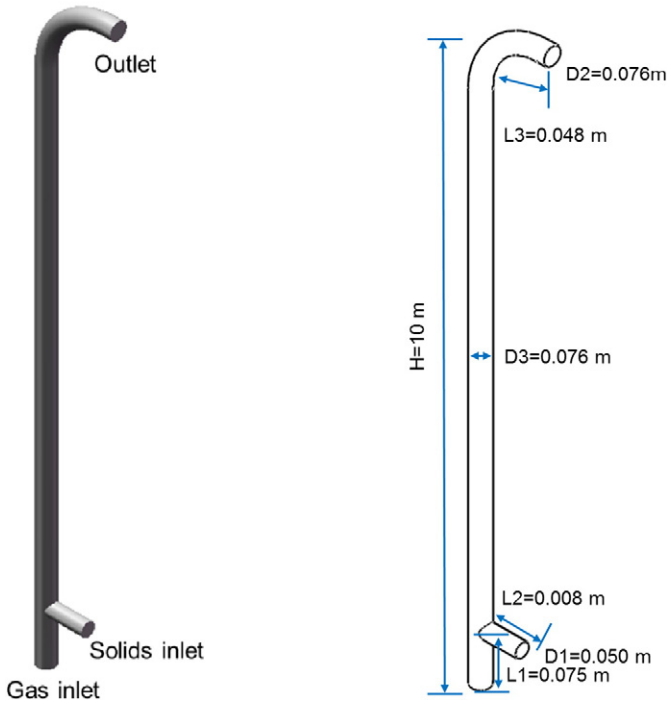


Fig. 2. Schematic of the 3D computational domain of the CFB riser.

### 2.3. Energy conservation equations

The energy conservation equation for the fluid phase was from O'Rourke [21], as shown below:

$$\frac{\partial(\theta_f \rho_f h_f)}{\partial t} + \nabla \cdot (\theta_f \rho_f h_f u_f) = \theta_f \left( \frac{\partial p}{\partial t} + u_f \cdot \nabla p \right) + \Phi - \nabla \cdot (\theta_f q) + \dot{Q} + S_h + \dot{q}_D \quad (3)$$

where  $h_f$  is the fluid enthalpy,  $Q$  is the energy source per volume,  $\Phi$  is the viscous dissipation. As stated by Snider et al. [19], there is no energy source when ignoring the viscous dissipation. The  $S_h$  represents the conservative energy exchange from the particle phase to the fluid phase,  $q$  is the fluid heat flux, as shown below:

$$q = -\lambda_f \nabla T_f \quad (4)$$

where  $\lambda_f$  is the fluid thermal conductivity, and it represents the sum of a molecular conductivity and an eddy-conductivity from Reynolds stress mixing. The eddy-conductivity is calculated by a turbulent Prandtl number correlation, as shown below:

$$Pr_t = \frac{C_p \mu_t}{\lambda_t} \quad (5)$$

where  $Pr_t$  is a standard value of 0.9,  $\dot{q}_D$  in Eq. (3) is the enthalpy diffusion term, as shown below:

$$\dot{q}_D = \sum_{i=1}^{N_s} \nabla \cdot (h_i \theta_f \rho_f D \nabla Y_{f,i}) \quad (6)$$

where  $i$  is gas-phase species,  $N_s$  is the summation of all gas species,  $h_{f,i}$  is the enthalpy of gas-phase species.

The gas-solids flow is compressible, and the pressure, enthalpy, temperature, density and mass fractions of gas phase are closely related through the state equation. In CPFD model, the partial pressure of gas

Table 2

System geometry and physical properties of CFB riser.

Parameter	Value
CFB riser diameter, $D$ (m)	0.076
CFB riser height, $H$ (m)	10.0
Solids inlet position, $L_1$ (m)	0.075
Solids inlet diameter, $D_1$ (m)	0.050
Solids inlet tube length, $L_2$ (m)	0.008
Outlet tube length, $L_3$ (m)	0.048
Particle diameter, $d_p$ ( $\mu\text{m}$ )	76.0
Particle density, $\rho_p$ ( $\text{kg}/\text{m}^3$ )	1780
Gas density, $\rho_g$ ( $\text{kg}/\text{m}^3$ )	1.1795
Gas viscosity, $\mu_g$ ( $\text{Pa}\cdot\text{s}$ )	$1.83 \times 10^{-5}$
Temperature, $T$ (K)	293.0
Grid number, $N_x \times N_y \times N_z$	$23 \times 425 \times 17$

species is given by the ideal gas state equation, as shown below:

$$P_i = \frac{\rho_f Y_{f,i} R T_f}{M w_i} \quad (7)$$

where  $T_f$  is the gas mixture temperature,  $R$  is the universal gas constant,  $M w_i$  is the molecular weight of gas species  $i$ , the gas thermodynamics pressure of total mean flow is related to the species pressure, as shown below:

$$P = \sum_{i=1}^{N_s} P_i \quad (8)$$

The mixture enthalpy is related to the species enthalpies and given by:

$$h_f = \sum_{i=1}^{N_s} Y_{f,i} h_i \quad (9)$$

The term  $C_p$  in Eq. (5) is the mixture specific heat at constant pressure, as shown below:

$$C_p = \sum_{i=1}^{N_s} Y_{f,i} C_{p,i} \quad (10)$$

where  $C_{p,i}$  is the specific heat of species  $i$ , and the species enthalpies  $h_i$  is a function of the fluid temperature  $T_f$ , as shown below:

$$h_i = \int_{T_{\text{ref}}}^{T_f} C_{p,i} dT + \Delta h_{f,i} \quad (11)$$

where the  $\Delta h_{f,i}$  is the heat formation of species  $i$  at the reference temperature  $T_{\text{ref}}$ .

For the energy conservation equation for the particle, it was assumed that the temperature is uniform across the whole particle,

Table 3

Simulation parameters and initial and boundary conditions used in CPFD.

Parameter	Value
Gas superficial velocity, $U_g$ (m/s)	7.0
Solids flux, $G_s$ ( $\text{kg}/(\text{m}^2 \cdot \text{s})$ )	200, 300
Packing limit	0.6
Maximum momentum redirection from collision	40%
Normal-to-wall momentum retention	0.99
Tangent-to-wall momentum retention	0.33
Solids volume fraction of inlet BCs	0.25
Simulation time, $t$ (s)	20
Initial time step, (s)	$5.0 \times 10^{-4}$
Pressure, $P$ (atm)	1.0
Initial ozone concentration, (ppm)	80–100
Ozone decomposition reaction rate, $kr$ ( $\text{s}^{-1}$ )	49.0

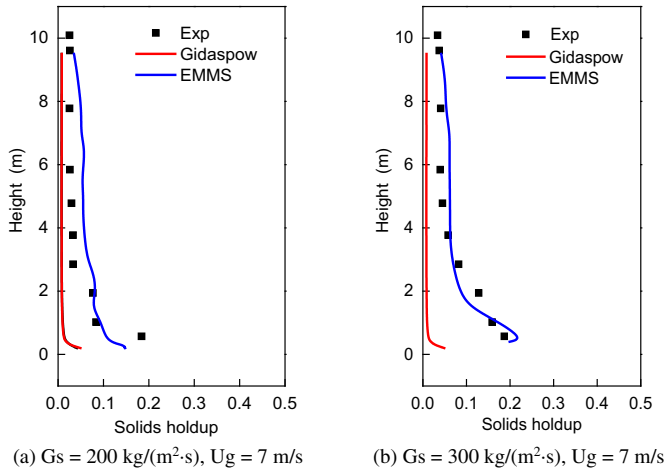


Fig. 3. Predicted axial profiles of solids holdup with different drag models.

which indicates that there is no heat release within the particle under the process of chemical reactions. In addition, during the process of chemical reactions, the heat release occurring on the particles' surfaces is part of the gas-phase energy, and the heat release has no effect on the surface energy balance. The lumped particle heat equation is shown:

$$C_v \frac{dT_p}{dt} = \frac{1}{m_p} \frac{\lambda_f Nu_{f,p}}{2r_p} A_p (T_f - T_p) \quad (12)$$

where  $C_v$  is the specific heat of particle,  $T_p$  is the particle temperature,  $Nu_{f,p}$  is the Nusselt number for describing the heat transfer from the fluid phase to the particle phase.

The energy exchange from the particle phase to the fluid phase is shown:

$$S_h = \iiint \left\{ m_p \left[ D_p (u_p - u_f)^2 - C_v \frac{dT_p}{dt} \right] - \frac{dm_p}{dt} \left[ h_p + \frac{1}{2} (u_p - u_f)^2 \right] \right\} dm_p du_p dT_p \quad (13)$$

where  $h_p$  is the particle enthalpy:

$$h_p = (2.0 + 1.2 \text{Re}^{0.5} \text{Pr}^{0.33}) \times \left( \frac{\lambda_f}{dp} \right) \quad (14)$$

#### 2.4. Ozone decomposition reaction kinetics

In order to validate the three-dimensional CPFDP model for simulating gas-solids chemical reactions in the CFB riser, the ozone

decomposition reaction was adopted as an example for illustration in the current study, since this reaction system is isothermal and only involves one reactant and one product. The ozone decomposition takes places on the active site of the catalyst surface as below:



In several previous studies [22,23], both the ozone decomposition and combination reactions were assumed to be isothermal and be first-order reactions with a constant ozone decomposition reaction rate. Since the first-order rate of decomposition mainly depends on the presence of active site of catalyst, the solids concentration was included into the kinetic rate. The consumption of ozone in the gas phase (the ozone decomposition reaction rate equation) is:

$$R_{\text{O}_3} = - \frac{k_r \theta_p \rho_g X_{\text{O}_3}}{M_{\text{O}_3}} \quad (16)$$

where  $R_{\text{O}_3}$  is the ozone decomposition reaction rate,  $k_r$  is the reaction rate constant based on the catalyst activity,  $\rho_g$  is the gas density,  $\theta_p$  is the particle volume fraction,  $X_{\text{O}_3}$  is the mole fraction of ozone,  $M_{\text{O}_3}$  is the molecular weight of ozone.

The air containing ozone was uniformly introduced into the riser from the bottom of the CFB riser at a fixed flow rate. The simulation parameters and initial and boundary conditions, including the initial ozone concentration in the fluidizing air, the ozone decomposition reaction rate constant used in CPFDP for numerical simulations were described in the following.

#### 2.5. Simulation setup

Fig. 1 showed the schematic diagram of the simulated CFB riser with Geldart A particles in the experiment of Wang [20]. This experimental CFB riser with an internal diameter of 0.076 m and a height of 10 m was used for the model validation. Fig. 2 illustrated the three-dimensional geometry of the CFB riser, which was discretized with a uniform grid size in each direction. Two cases with a same superficial gas velocity of 7 m/s and different solids circulating fluxes of 200 and 300 kg/(m<sup>2</sup>·s), respectively, were studied. The homogeneous mixture of air and ozone was uniformly fed into the riser through the bottom of the riser while the catalyst particles were from the side near the bottom at a constant mass flow rate. The initial ozone concentration in the fluidizing gas was set at 80–100 ppm. Initially, there are no catalyst particles inside the riser. In the experiment, to map the entire cross-section of the riser, the measuring ports at the height of 0.57, 1.02, 1.94, 2.85, 3.77, 4.78, 5.84, 7.78 and 9.61 m were installed to determine the ozone concentration profiles in axial direction, as well as at the radial direction of  $r/R = 0, 0.316, 0.548, 0.707, 0.837$  and  $0.950$ . The catalyst for ozone decomposition in their experiment was primarily composed of

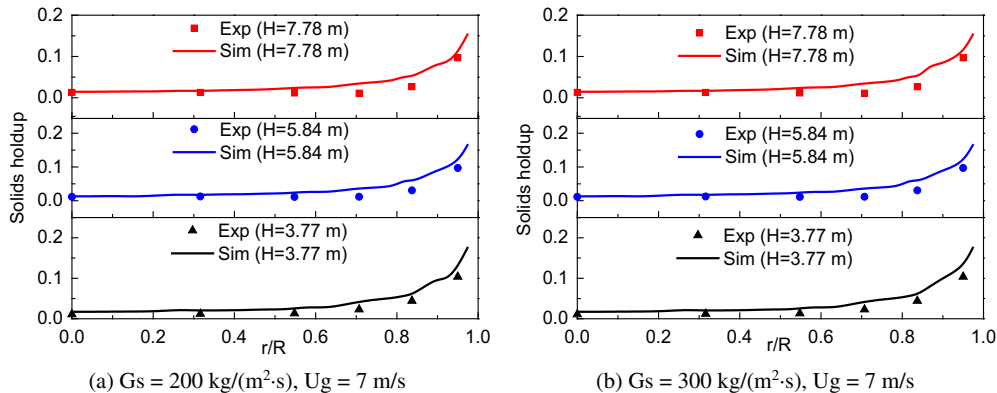


Fig. 4. Radial profiles of solids holdup with EMMS-based drag model.

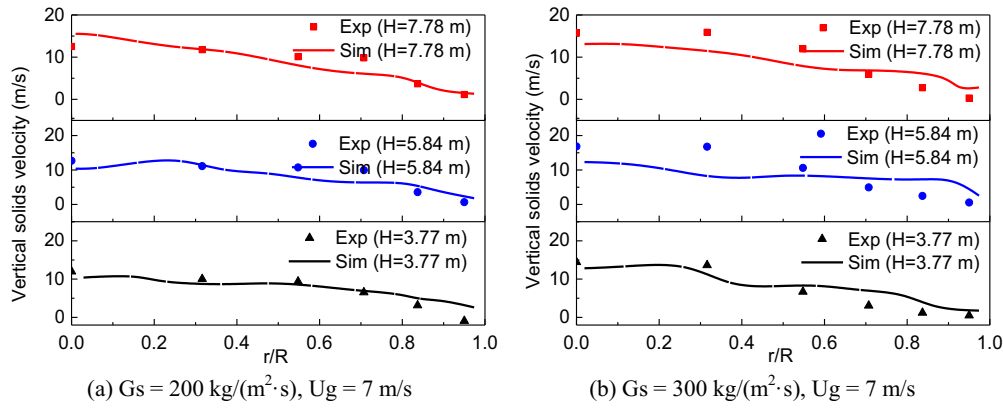


Fig. 5. Radial profiles of vertical solids velocity with EMMS-based drag model.

porous amorphous aluminum hydrosilicate, and then was activated by impregnating in a 40% (wt) solution of ferric nitrate overnight. Finally, the soaked particles were dried and calcinated in an oven with a hood at 450 °C for 4 h until no  $\text{NO}_2$  released. During the calcinations, the ferric nitrate was converted into ferric oxide. The ferric oxide was the active component in the ozone decomposition reaction. The catalyst has a Sauter mean diameter of 76  $\mu\text{m}$  and a density of 1780  $\text{kg}/\text{m}^3$ . The ozone decomposition reaction rate of the catalyst is at a constant of 49.0  $\text{s}^{-1}$ , which was regularly checked using a fixed bed reactor in the experiment. Li et al. [23] and Kong et al. [24] reported that there was a resistance during the catalytic ozone decomposition reaction process when the ozone was transferred from the cluster surface to cluster core, therefore, a modification factor was introduced to consider the effect of clusters. In this paper, the suitable value of modification factor was set to be 0.4. The outlet boundary condition of gas and solids was at atmospheric pressure. A time step of  $5.0 \times 10^{-4}$  s with 100 iterations per time step was applied throughout simulations and the simulations

were carried out for 20 s. The detailed system geometry and physical properties, simulation parameters and initial and boundary conditions of the CFB riser used in CPFD were summarized in Tables 2 and 3.

### 3. Results and discussion

#### 3.1. Selection of an appropriate drag model

In gas-solids systems, the interactions between gas and solids play a dominant role in affecting the gas-solids flow behaviors. Therefore, it is important to select an appropriate drag model for accurately describing the gas-solids interactions in the CFD simulation of gas-solids systems. At the flow conditions of a superficial gas velocity of 7 m/s and solids circulating fluxes of 200 and 300  $\text{kg}/(\text{m}^2 \cdot \text{s})$ , respectively, the effects of the drag models (EMMS-based drag model vs. Gidaspow drag model) on the gas-solids flow hydrodynamics were analyzed by making comparison between the simulation results of the time-averaged axial profiles

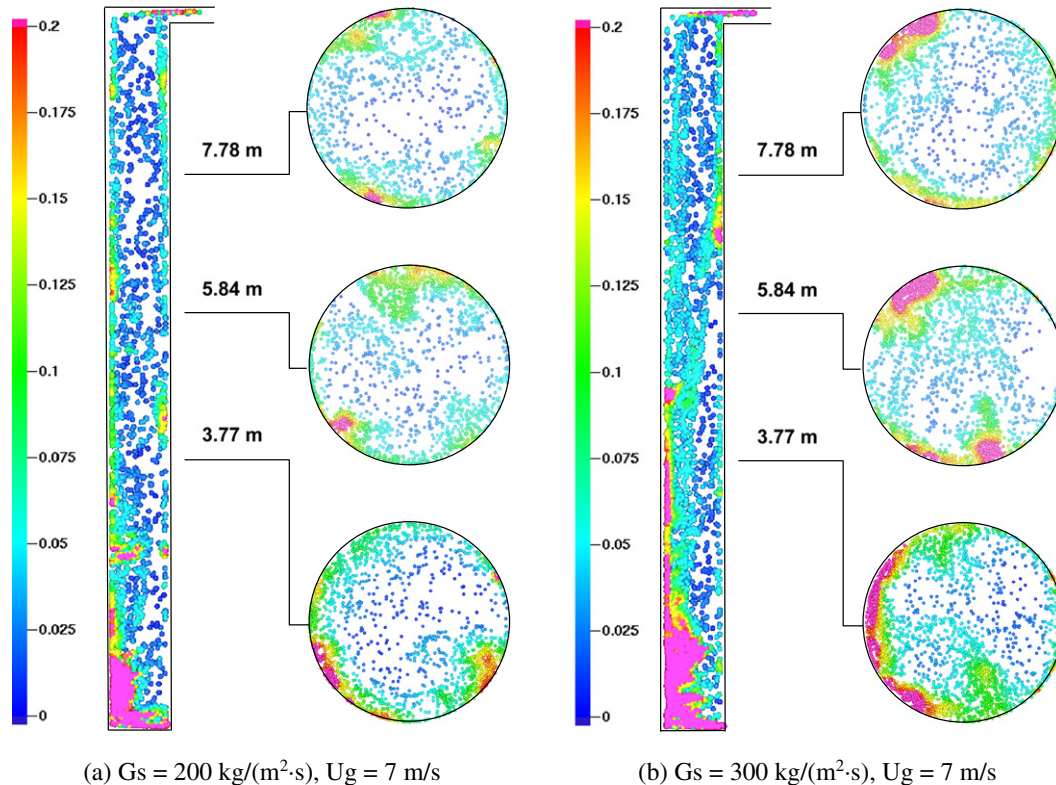


Fig. 6. Instantaneous distribution of solids holdup (the height of riser is scaled down by a factor of 10, the size of particle is scaled up by a factor of 8).

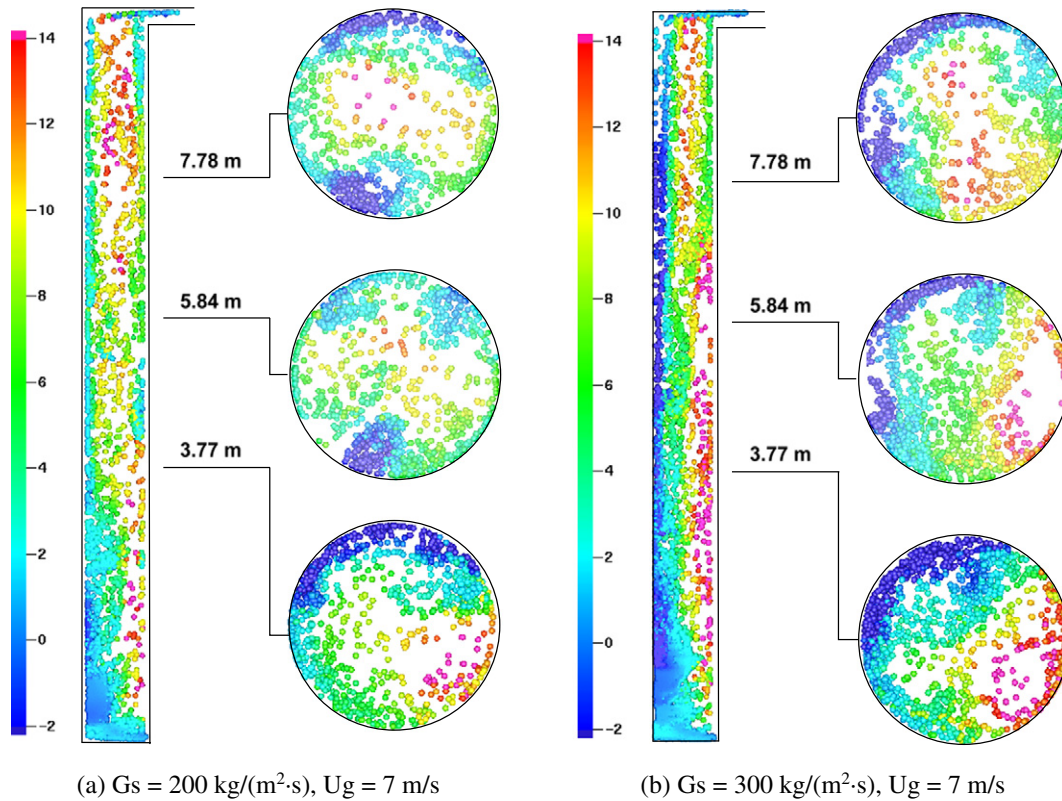


Fig. 7. Instantaneous distribution of vertical solids velocity (the height of riser is scaled down by a factor of 10, the size of particle is scaled up by a factor of 8).

of solids holdup and the experimental data from the literature [20]. As shown in Fig. 3, it can be seen that the simulation results with the EMMS-based drag model can give more accurate results than the Gidaspow drag model. Chen et al. [25] also indicated that the drag model (i.e. EMMS) taking into account the local heterogeneous structure (i.e. clusters) in the CFB risers would obtain more accurate results than the homogeneous drag model (e.g. Gidaspow drag model) without considering the local heterogeneity in the CPFD simulations. Other researchers also found that the EMMS-based drag model had a better performance than the drag model that was without the consideration of local heterogeneous structure [16,26,27].

### 3.2. Gas-solids flow hydrodynamics

Figs. 4 and 5 display the comparison between the simulation results with the EMMS-based drag model and the experimental data with respect to the time-averaged radial profiles of solids holdup and solids vertical velocity at three axial positions ( $H = 3.77, 5.84, 7.78$  m) at two different operating conditions. As shown in Figs. 4 and 5, reasonable agreement between the simulation results with the EMMS-based drag model and the experimental data was achieved. Yang et al. [28] indicated that the EMMS-based drag model considered and resolved the heterogeneous structure, the gas-solids interactions inside the dense phase and the dilute phase, and the interactions between the clusters and the surrounding dilute phase. In general, three-dimensional CPFD approach with the EMMS-based drag model can give relatively accurate predictions for the gas-solids flow hydrodynamics in the CFB riser. Hence, the EMMS-based drag model was used in the following study. In addition, the radial profiles were predicted to show “core-annulus” flow pattern with a dense annular falling down (though not obvious in both the experiment data and the simulation results as shown in Fig. 5, which shows the averaged results across the cross-section at a specific height of the 3D riser) close to the wall and a dilute core rapidly rising at the center of the riser. In the literature [29], it was reported that the strong and complex interactions between solids and wall can affect solids flow behaviors which would lead to downward flow of solids near the wall area. Li and Guenther [30] reported that the clusters' continuous development, breaking up, and falling down near the wall region were responsible for the “core-annular” flow pattern. The above analysis showed that both the wall effects and the clusters contribute to the “core-annular” flow structure in CFB riser.

Figs. 6 and 7 show instantaneous distributions of solids holdup and solids vertical velocity. As can be seen from these figures, it was predicted that solids showed higher concentration and lower vertical velocity

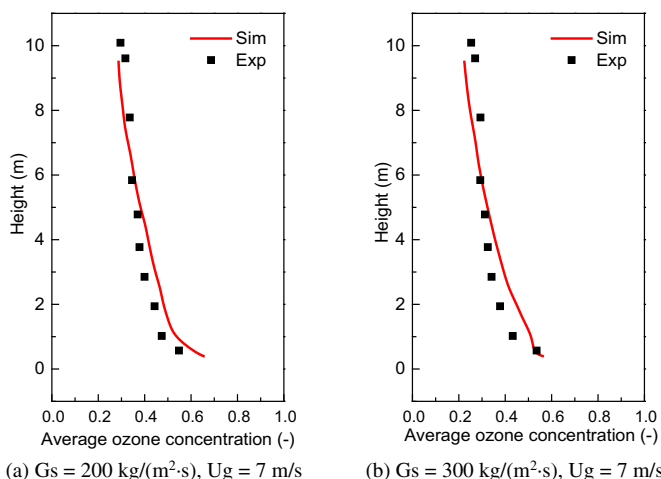


Fig. 8. Axial profiles of dimensional ozone concentration.

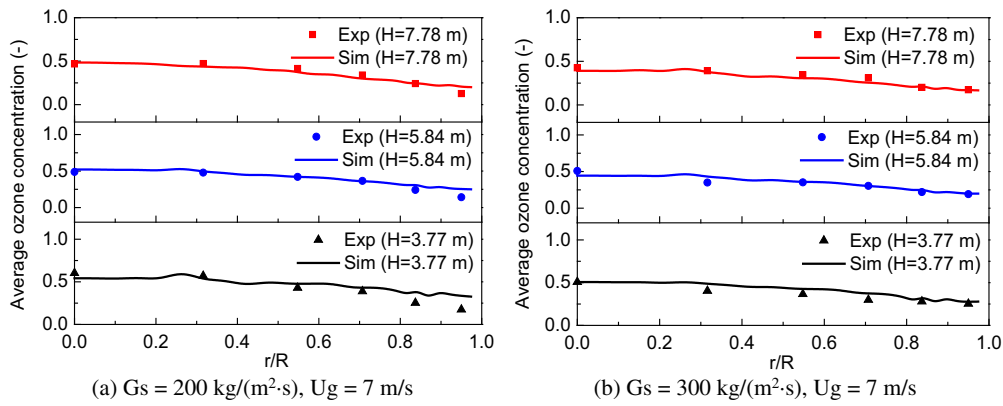


Fig. 9. Radial profiles of dimensional ozone concentration.

(or even downward flow) near the wall of the riser, which corresponds to the averaged results as shown in Figs. 4 and 5. As also shown in these figures, the radial profiles of solids holdup and solids vertical velocity presented non-uniform characteristics at different cross sections, and particles tended to gather to form clusters, especially at the bottom region and near the wall region. Agrawal et al. [31] and Shi et al. [32] indicated that an instability attributed to the damping of the particles' fluctuating motion by the interstitial fluid and inelastic collisions between particles, and an inertial instability attributed to the relative motion between the gas and solid phases lead to the formation of clusters. Due to the existence of more clusters near the wall, the gas tends to flow along the center of the riser, which results into higher solids velocity and lower solids holdup at the center of the riser. In addition, it can be seen that under the same superficial gas velocity, with increasing the solids circulation rate from 200 to 300 kg/(m<sup>2</sup>·s), solids holdup increased at each axial position, and more particles and higher solids holdup were present near the wall region. This phenomenon indicates

that the operating conditions can have significant influence on the gas-solids flow hydrodynamics.

### 3.3. Reaction characteristics

The three-dimensional CFPD approach with the EMMS-based drag model was used for studying the catalytic ozone decomposition process in a CFB riser through coupling with the reaction kinetics. Figs. 8 and 9 compare the predicted axial and radial profiles of the time-averaged ozone concentration with the experimental data under two different operating conditions. In these figures, ozone concentrations were presented in the form of "dimensionless concentration" defined by dividing the actual ozone concentration by the initial concentration at the riser inlet. It can be seen that the simulation results were in good agreement with the experimental results at each axial and radial positions. Therefore, three-dimensional CFPD approach with the EMMS-based drag model and with the chemical reaction kinetics can be employed to

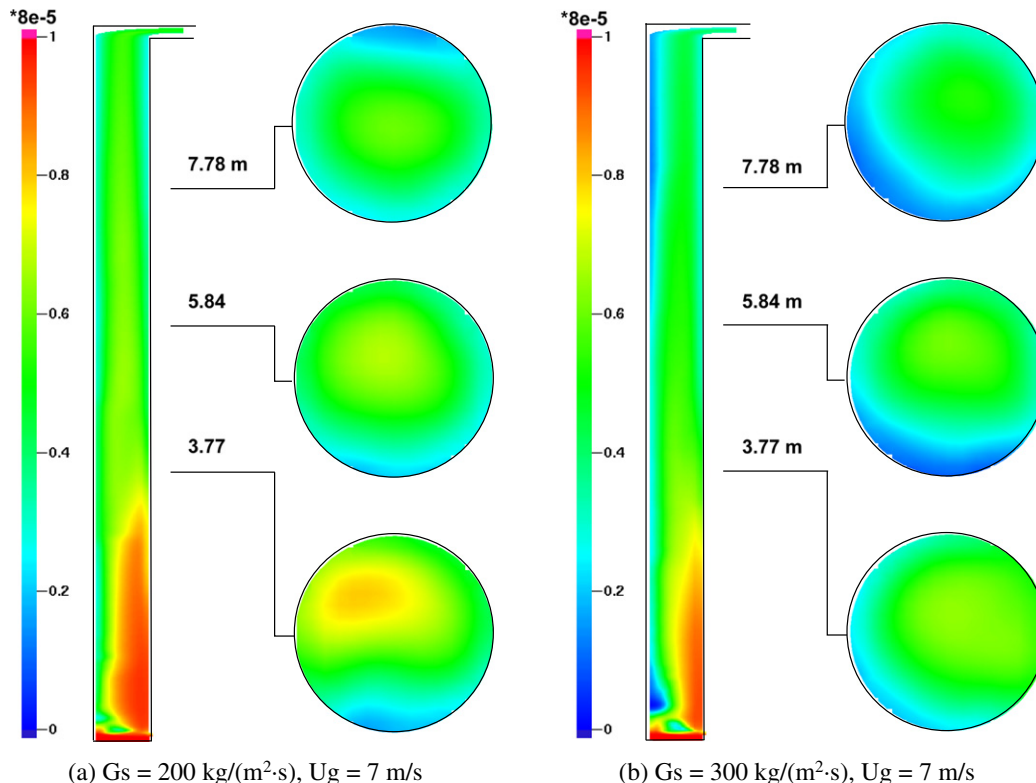


Fig. 10. Time-averaged contour plots of ozone concentration (the height of riser is scaled down by a factor of 10).

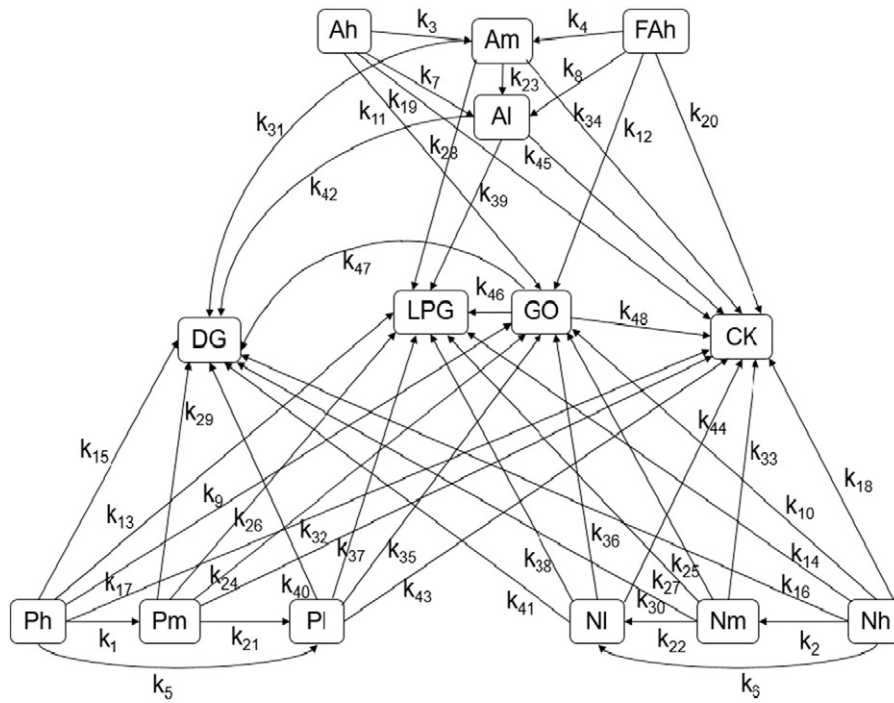


Fig. 11. Reaction network of the 14-lump kinetic cracking model.

analyze the gas-solids flow hydrodynamics and chemical reaction characteristics of the CFB riser reactor with Geldart A particles. In addition, as shown in Fig. 8, ozone concentration rapidly decreased at the entrance area, which indicates that higher ozone conversion rate appeared in the bottom feeding region where the initial gas-solids contacting occurs in the riser. Therefore, during the chemical reaction process in the CFB riser, the initial gas-solids contacting plays a key role, and more attention needs to be paid on the entrance design of the CFB riser.

Fig. 10 shows the time-averaged contour of ozone concentration. It can be seen that, except at the bottom feeding region, the overall profiles of the ozone concentration were consistent with the corresponding profiles of the solids holdup. The higher ozone concentration occurred in the center region of riser, where solids (catalyst) concentration was low. In addition, it can be seen that under the same superficial gas velocity, the increase of the solids circulation rate from 200 to 300 kg/(m<sup>2</sup>·s) led to the increase of solids holdup and the decrease of ozone concentration at each axial position. This finding indicates that the ozone decomposition reaction in the CFB riser is largely influenced by the gas-solids flow behaviors.

Table 4  
Components of the 14-lump kinetic model.

Lump symbol	Lump	Boiling range
Ph	Heavy paraffinics	500 °C
Pm	Medium paraffinics	350–500 °C
Pl	Light paraffinics	221–350 °C
Nh	Heavy naphthenics	500 °C
Nm	Medium naphthenics	350–500 °C
Nl	Light naphthenics	221–350 °C
FAh	Heavy aromatics in resin and asphaltene	500 °C
Ah	Heavy aromatics except FA <sub>h</sub>	500 °C
Am	Medium aromatics	350–500 °C
Al	Light aromatics	221–350 °C
GO	Gasoline	C5–221 °C
LPG	Liquid petroleum gas	C3 + C4
DG	Dry gas	C1 + C2 + H <sub>2</sub>
CK	Coke	

### 3.4. Application on industrial FCC riser

The above results showed that the three-dimensional CPFD approach with the EMMS-based drag model and with the chemical reaction kinetics can be employed to analyze the gas-solids flow hydrodynamics and chemical reaction characteristics of the CFB riser reactor with Geldart A particles. Therefore, based on the above research results, the CPFD approach with the EMMS-based drag model and with the consideration of a 14-lump kinetic model was applied to investigate the gas-solids flow hydrodynamics and cracking reaction characteristics of a large-scale industrial FCC riser reactor with a processing capacity of 1.0 × 10<sup>6</sup> tons/year.

#### 3.4.1. Catalytic cracking reaction kinetic model

With the rapid mixing and heat transfer between the cold feedstock oil and the hot catalyst in the riser, conversion of heavier hydrocarbons to lighter products takes place on the active site of hot catalyst. At the same time, many side reactions, such as hydrogen transfer and coking also occur with the catalyst, droplets, and gas (hydrocarbon vapor and steam) concurrently flowing upward along the FCC riser. In general, there are numerous complex reactions in the FCC processes. Therefore, it is impossible to consider all the elemental reactions and their reaction rates for a large-scale industrial reactor in the CPFD simulation. The common approach of including complex chemistry, in a computationally tractable way, is to adopt the lumped model to describe the reaction kinetics of catalytic cracking. In the lumped model, pseudo components are chosen to characterize the whole mixture of the catalytic cracking of petroleum fractions. In this study, a 14-lump reaction kinetic model [33, 34] was applied to describe catalytic cracking reactions. The detailed reaction scheme describing the reaction network of the 14-lump FCC kinetic model is shown in Fig. 11. The components in the 14-lump kinetic model and the kinetic parameters are shown in Tables 4 and 5, respectively.

The reaction rate of lump *i* is given by:

$$r_i = -A_0 \cdot \frac{\Phi(C_c)}{1 + k_h C_{Ah}} \cdot \frac{\rho_g \rho_p}{\theta_g} K_i Y_i \quad (17)$$

**Table 5**  
Kinetics and activation energy constants of the 14-lump kinetic model.

Path no.	Path	Frequency factor, $k_0$ ( $\text{m}^3/\text{kg}_{\text{cat}}/\text{s}$ )	Activation energy, $E$ (kJ/kg)	Path no.	Path	Frequency factor, $k_0$ ( $\text{m}^3/\text{kg}_{\text{cat}}/\text{s}$ )	Activation energy, $E$ (kJ/kg)
1	Ph → Pm	18.77	7.21e+4	25	Nm → GO	0.4092	3.04e+4
2	Nh → Nm	19.25	7.21e+4	26	Pm → LPG	1.506	4.32e+4
3	Ah → Am	1.817	7.21e+4	27	Nm → LPG	0.5742	4.32e+4
4	FAh → Am	0.5514	7.21e+4	28	Am → LPG	0.0438	2.76e+4
5	Ph → Pl	16.38	7.21e+4	29	Pm → DG	5.491	6.32e+4
6	Nh → NI	17.05	7.21e+4	30	Nm → CK	2.013	6.32e+4
7	Ah → Al	1.617	7.21e+4	31	Am → DG	0.0324	5.00e+4
8	FAh → Al	0.4342	7.21e+4	32	Pm → CK	1.704	5.00e+4
9	Ph → GO	0.2266	3.04e+4	33	Nm → CK	1.061	5.00e+4
10	Nh → GO	0.1374	3.04e+4	34	Am → CK	5.611	5.44e+4
11	Ah → GO	0.0136	3.76e+4	35	Pl → GO	1.257	3.04e+4
12	FAh → GO	0.0054	3.76e+4	36	NI → GO	1.986	3.04e+4
13	Ph → LPG	5.77	4.32e+4	37	Pl → LPG	2.258	4.32e+4
14	Nh → LPG	6.20	4.32e+4	38	NI → LPG	1.506	4.32e+4
15	Ph → DG	63.18	6.32e+4	39	Al → LPG	0.033	2.76e+4
16	Nh → DG	64.99	6.32e+4	40	Pl → DG	15.20	6.32e+4
17	Ph → CK	3.366	5.00e+4	41	NI → DG	10.14	6.32e+4
18	Nh → CK	4.754	5.00e+4	42	Al → DG	0.0498	3.76e+4
19	Ah → CK	41.82	5.44e+4	43	Pl → CK	0.1363	5.00e+4
20	FAh → CK	40.50	5.44e+4	44	NI → CK	0.1491	5.00e+4
21	Pm → Pl	833.90	7.21e+4	45	Al → CK	0.8254	5.44e+4
22	Nm → NI	944.00	7.21e+4	46	GO → DG	1374.00	1.18e+4
23	Am → Al	773.80	7.21e+4	47	GO → DK	343.40	1.18e+4
24	Pm → GO	1.263	3.04e+4	48	GO → CK	0.066	5.61e+4

where  $A_0$  is the correction coefficient of the initial catalyst activity, which is equal to the ratio of the consumed catalyst activity to that of the employed catalyst in the kinetic experiment,  $C_c$  is the content of coke on FCC catalysts,  $k_h$  is the adsorption coefficient of aromatics,  $\Phi(C_c)$  is the decay function of the catalyst owing to the coke deposition on the catalyst surface, and is described by the following equation:

$$\Phi(C_c) = (1 + 0.51C_c)^{-2.78} \quad (18)$$

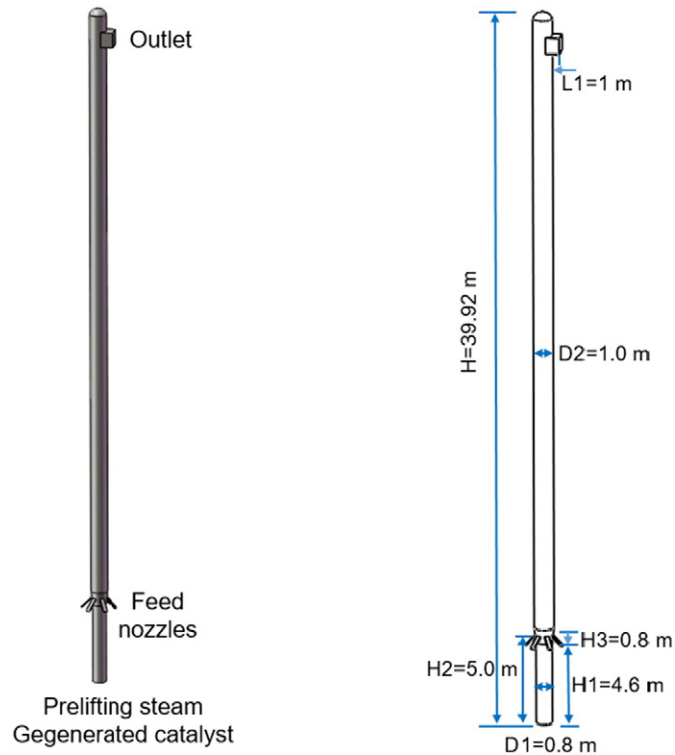


**Fig. 12.** Schematic of the 3D computational domain of the industrial FCC riser.

### 3.4.2. Simulation setup

Fig. 12 illustrated the three-dimensional computational geometry of the FCC riser, which was discretized with a uniform grid size in each direction. This large-scale industrial FCC riser was composed of prelifting zone, feed injection zone, and main-riser zone. Prelifting steam and the regenerated FCC catalysts were fed into the riser from the bottom of the prelifting zone with an internal diameter of 0.8 m and a height of 4.6 m. As prelifting steam and catalysts moved upward along the prelifting zone in the axial direction, they encountered with the feedstock which was injected with atomizing steam through a set of feed oil injection nozzles. All the nozzles have the same geometric structure and size with a length of 1.0 m and a rectangular cross-sectional area of 0.204 m × 0.051 m. The nozzle is evenly distributed around an enlarged-diameter section of the riser, or the “main-riser”, which has an internal diameter of 1.0 m and a height of 35.32 m. In this study, the capacity of feed oil is 152 t/h, the amount of atomizing steam is 9.6 t/h, the catalyst circulating rate is 1156 t/h, the catalyst to oil ratio is about 7–8, and the atomizing steam and prelifting gas temperatures are 290 and 520 °C, respectively. Our previous research [35,36] found that the feedstock oil can be instantly vaporized when it comes into

**Table 6**  
System geometry and physical properties of commercial FCC riser.

Parameter	Value
Prelifting zone diameter, $D1$ (m)	0.8
Prelifting zone height, $H1$ (m)	4.6
Main-riser diameter, $D2$ (m)	1.0
FCC riser height, $H$ (m)	39.92
Outlet tube length, $L1$ (m)	6.176
Outlet tube cross-section area, ( $\text{m}^2$ )	0.64
Transition section height, $H3$ (m)	0.8
Jet nozzle height, (m)	5.0
Jet nozzle number	6
Jet nozzle angle, ( $^\circ$ )	45
Jet nozzle length, (m)	1.0
Jet nozzle cross-sectional area, $A2$ ( $\text{m}^2$ )	$0.204 \times 0.051$
Particle diameter, $d_p$ ( $\mu\text{m}$ )	70
Particle density, $\rho_p$ ( $\text{kg}/\text{m}^3$ )	1500
Gas density, $\rho_g$ ( $\text{kg}/\text{m}^3$ )	1.1795
Gas viscosity, $\mu_g$ ( $\text{Pa}\cdot\text{s}$ )	$1.83 \times 10^{-5}$
Temperature, $T$ (K)	823
Grid number, $N_x \times N_y \times N_z$	$18 \times 307 \times 14$

**Table 7**  
Simulation parameters and initial and boundary conditions used in CPF.D.

Parameter	Value
Feed oil, (t/h)	152.0
Feed oil composition (mass fraction)	
Ph	0.208391
Nh	0.026364
Ah	0.046527
Fh	0.031018
Pm	0.315629
Am	0.125847
Nm	0.196224
H <sub>2</sub> O	0.05
Atomizing steam, (t/h)	9.6
Pre lifting gas, (kg/h)	4070.0
Catalyst circulating rate, (t/h)	1156.0
Catalyst to oil ratio	7.0–8.0
Material temperature, (K)	493.0
Atomizing steam temperature, (K)	563.0
Prelifting gas temperature, (K)	793.0 ± 2.0
Mixing temperature, (K)	823.0
Close pack volume fraction	0.6
Maximum momentum redirection from collision	40%
Normal-to-wall momentum retention	0.9
Tangent-to-wall momentum retention	0.33
Particle feed mass flow rate, kg/(m <sup>2</sup> ·s)	321.0
Simulation time, t (s)	20
Initial time step, (s)	1 × 10 <sup>-4</sup>
Pressure, P (atm)	1

contact with the hot catalyst particles from the regenerator. Therefore, the influence of the feedstock vaporization process was not considered into the simulation. The FCC catalyst has a mean diameter of 70 μm and a density of 1500 kg/m<sup>3</sup>. The outlet boundary conditions of gas and solids were set to be atmospheric pressure. A time step of 1.0 × 10<sup>-3</sup> s with 100 iterations per time step was applied throughout simulations and the simulations were carried out for 20 s. Initially, the solids volume fraction was set to be zero. The detailed system geometry and physical properties of gas and solids, simulation parameters and initial and boundary conditions were summarized in Tables 6 and 7.

#### 3.4.3. Grid independency test

In this study, to confirm that the simulation results were grid-independent in simulating the industrial FCC riser, simulation results at three grid resolutions with 5 × 10<sup>4</sup> cells (coarse mesh), 1.0 × 10<sup>5</sup> cells (medium mesh), 1.4 × 10<sup>5</sup> cells (fine mesh), respectively, were compared with respect to the predicted time-averaged axial distributions of the solids holdup, as shown in Fig. 13. From this figure, it can

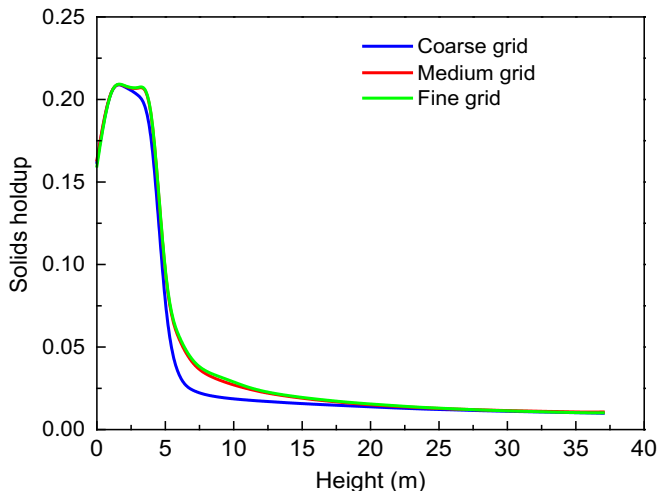


Fig. 13. The effect of the grid resolutions on the axial distributions of solids holdup.

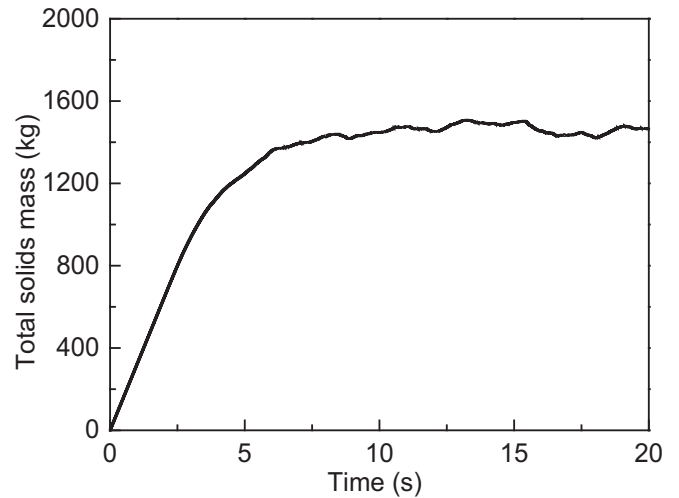


Fig. 14. Time evolution of the total particle mass in the CFB riser.

be seen that the simulation with medium mesh and with fine mesh predicted similar results, while the results using the coarse mesh deviated, to some extent, from the results using the medium mesh and the fine mesh. These results indicate that the medium mesh was already sufficiently fine for providing mesh independent results. Therefore, the medium mesh was applied in the following.

#### 3.4.4. Gas-solids flow hydrodynamics

Before analyzing the simulation results, it is necessary to make sure that the gas-solids flow has reached a statistically steady state. The total mass of solids inside the riser as a function of time, as shown in Fig. 14, was selected as a parameter to check whether the simulation has reached steady state. From this figure, it can be seen that, after 10 s, the total solids mass tended to be stable, indicating that the simulation tended to reach a statistically steady state. Therefore, the simulation results at the time of 10–20 s were statistically averaged in the following.

Fig. 15 shows the time-averaged axial profiles of solids holdup and solids vertical velocity. In the prelifting section, particles being slowly fed into the system from the solids inlet tended to be at loosely packing state. Therefore, it is reasonable that extremely high solids holdup and low solids velocity occurred in the prelifting section. However, the solids holdup promptly decreased and solids velocity rapidly increased near the feedstock injection point, and then the solids holdup almost leveled off in the developed region of the FCC riser reactor. This

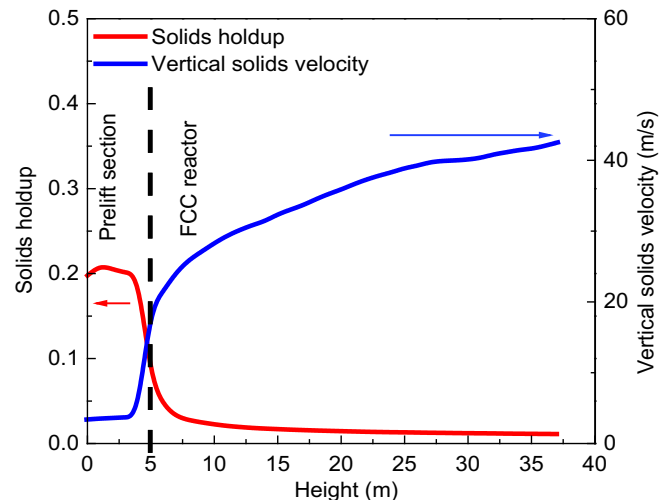


Fig. 15. Axial profiles of solids holdup and vertical solids velocity.

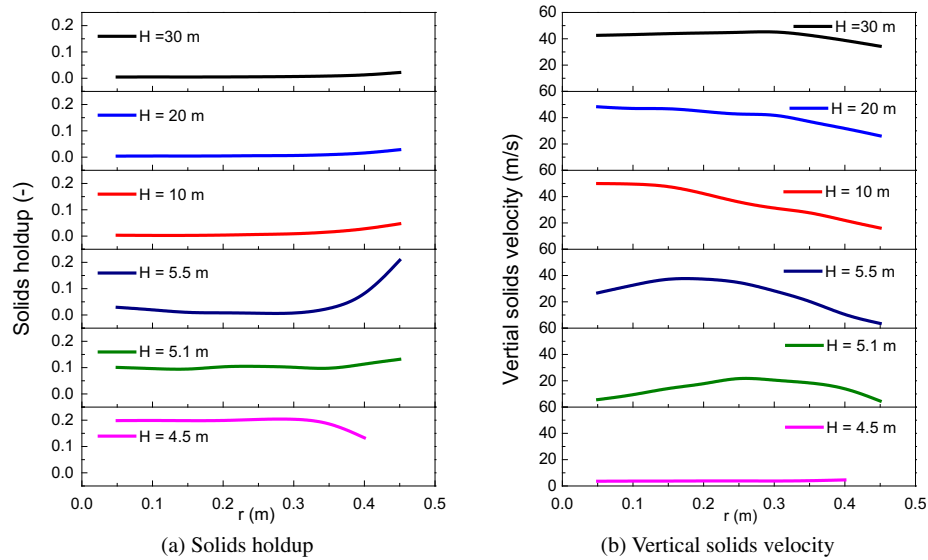


Fig. 16. Radial profiles of solids holdup and vertical solids velocity.

phenomenon can be attributed to two main reasons. The first reason is that, the upward catalyst particles are entrained and accelerated by the high-velocity prelifting steam, leading to the increase of solids velocity and the decrease of solids holdup along the height of the FCC riser reactor. Another more important reason is that the prompt vaporization of feedstock droplets and the rapid occurrence of thermal and catalytic cracking reactions of the feedstock near the injection point result in rapid increase of gas volume. It is generally believed that the effect of chemical reactions on gas-solids flow hydrodynamics is significant for gas-solids fluidized beds. For instance, Li et al. [22] investigated the

effect of gas volume change caused by chemical reactions on the flow hydrodynamics in a fluidized bed reactor. They illustrated that the influence of gas volume change, which is usually due to the chemical reaction, on gas-solids flow hydrodynamics (e.g. bed expansion, voidage, bubble size, bubble frequency, and inventory), was significant. Fig. 15 indicates that the gas volume rapidly increased near the feedstock injection point, which is due to the vaporization of feedstock droplets and the thermal and catalytic cracking reactions of the feedstock. Therefore, along the FCC riser height, the variation of gas volume has a profound impact on solids holdup and velocity. Consequently, the increase of the solids velocity and the decrease of the solids holdup due to the increase of the gas volume were originally attributed to the vaporization and the thermal and cracking reactions of feedstock in the FCC riser reactor.

Fig. 16 shows the time-averaged radial profiles of solids holdup and vertical solids velocity at the height of 4.5, 5.1, 5.5, 10, 20, 30 m. This figure shows that higher solids holdup and lower solids velocity occurred at  $H = 4.5$  m and 5.1 m, and then the solids holdup promptly decreased and the solids velocity rapidly increased near the feedstock injection point, which has already been discussed in Fig. 15. In addition, it can be found that at the height of 4.5 m, the dilute core structure was not located centrally, and instead, it shifted towards the wall as shown in Fig. 16a. This phenomenon can be attributed to the jet effects, although the jet effects quickly disappeared and the core-annular flow pattern was formed in a short distance above the jet zone. At the height of 10 m and above, uniform radial profiles can be observed, which indicates that the gas-solids flow has reached the fully developed state where the radial distributions of solids holdup and solids velocity remained relatively unchanged along the riser height.

Table 8

Comparison of simulation results and process data of products' mass fraction at riser outlet.

Product	Simulation results (wt%)	Industrial data (wt%)	Errors	
			Absolute	Relative
Dry gas	3.77	3.81	-0.04	-1.04
LPG	11.79	13.70	-1.91	-13.94
Gasoline	35.16	35.86	-0.70	-1.96
Diesel oil	28.15	28.72	-0.57	-1.98
H <sub>2</sub> O	5.0	5.0	-	-

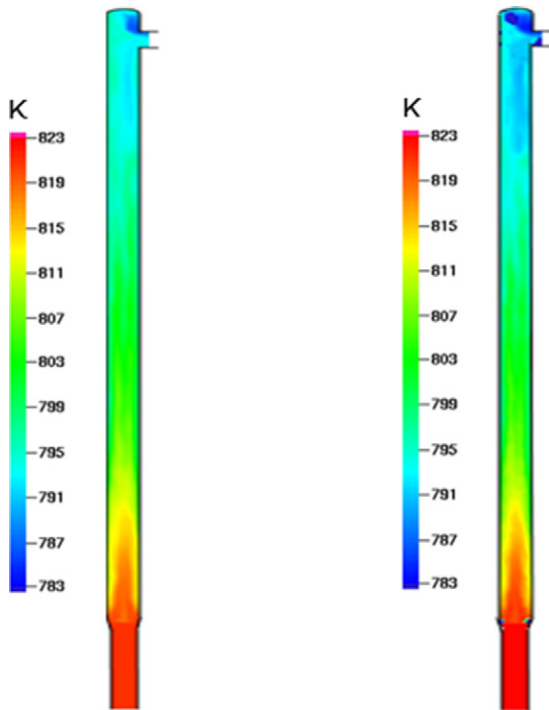


Fig. 17. Time-averaged distributions of gas temperature and solids temperature (The height of riser was scaled down by a factor of 2.).

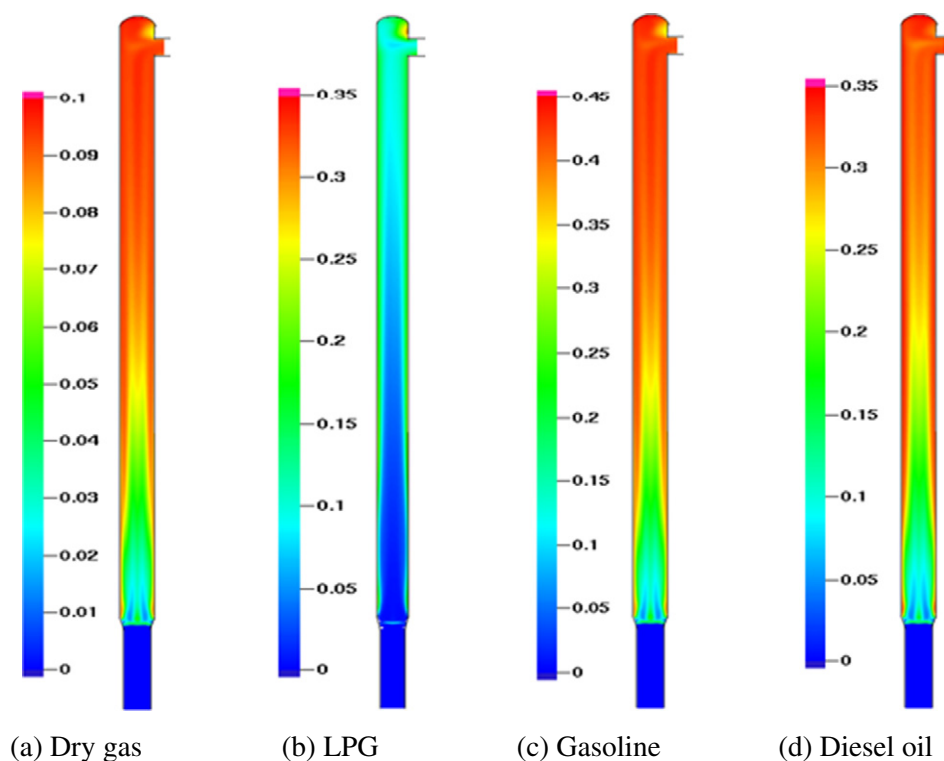


Fig. 18. Time-averaged distributions of products concentration (The height of riser was scaled down by a factor of 2.).

#### 3.4.5. Cracking reaction characteristics

Fig. 17 presents snapshots for the distributions of solids and gas temperatures in the riser reactor. It should be mentioned that the temperatures of any individual particles were also tracked with the CPFD method, although were not presented here, and their overall distribution was similar to that in Fig. 17(b). As described in Fig. 17, in the bottom region of the riser reactor, the solids and gas temperatures were higher, however, their temperatures rapidly decreased along the height of riser reactor. These results show that the catalytic reactions promptly happened in the injection section and the catalytic reactions were endothermic. In addition, it can be found that higher solids and gas temperatures were present in the center region compared to those near the wall region. This phenomenon can be due to the fact that higher catalysts (solids) concentration is present near the wall region, which provides more opportunities for the contact and mixing between catalysts and oil feedstock. Therefore, endothermic cracking reactions mainly occur near the wall region.

Table 8 shows the comparison of the predicted product distributions and the industrial data. It can be seen that the simulation results were in reasonable agreement with the industrial data, and the errors between the simulation and industrial data can be acceptable. This comparison indicates that the gas-solids flow, heat transfer, and chemistry behaviors in large-scale commercial and complex three-dimensional FCC riser reactor can be described by adopting the CPFD methodology.

Fig. 18 presents the snapshots of axial and radial profiles of concentrations of dry gas, liquefied petroleum gas (LPG), gasoline, and diesel oil respectively. Distributions of the products concentrations on any individual particles were also predicted, although were not shown here, and their overall distributions were similar to those in this figure. As shown in Fig. 18a–d, the distributions of products concentrations had typical annular-core features and changed gradually along the height of the FCC riser reactor. These phenomena were similar to the distributions of solids holdup and the distribution of solids and gas temperatures, indicating that heat transfer, mass transfer and chemical reaction characteristics in the FCC riser are closely related to the gas-solids flow hydrodynamics.

#### 4. Conclusions

In this work, the CPFD approach based on the MP-PIC method was applied to study the hydrodynamics and chemical reaction characteristics in CFB riser reactors with Geldart A particles. The CPFD approach was capable of tracking the coupled flow-reaction behaviors on the scales ranging from an individual particle to the whole reactor.

Firstly, the CPFD approach based on the EMMS drag model was used to predict the gas-solids flow hydrodynamics in a three-dimensional CFB riser with Geldart A particles. The ability of the CPFD approach in studying multiphase flow-reaction systems was further demonstrated by studying the ozone decomposition in a CFB riser reactor. In addition, the CPFD model was further extended to reveal the coupled flow-reaction behaviors in an industrial FCC riser reactor with a processing capacity of  $1.0 \times 10^6$  tons/year. Simulation results with respect to the products distributions from the FCC riser reactor were in reasonable agreement with the industrial data. It was demonstrated that the effect of chemical reactions on gas-solids flow hydrodynamics in the FCC riser was significant, i.e. the rapid increase of the gas-volume near the feedstock injection point due to the vaporization of feedstock droplets and their thermal and catalytic cracking reactions. It was found that solids holdup promptly decreased and solids velocity rapidly increased near the feedstock injection section. In addition, the distributions of solids holdup, solids and gas temperatures, and products concentrations showed annular-core features and strong inhomogeneous characteristics at different cross sections of the FCC riser reactor, indicating that the heat transfer, mass transfer and chemical reaction characteristics in the FCC riser were closely related to the gas-solids flow hydrodynamics. In summary, in the future, the gas-solids flow, heat transfer, and chemistry behaviors in a large-scale industrial and complex three-dimensional FCC riser reactor with Geldart A particles can be described in detail by adopting the CPFD method.

### Nomenclature

A	particle acceleration, $\text{m}\cdot\text{s}^{-2}$
$A_0$	correction coefficient of the initial catalyst activity
$C_C$	content of coke on FCC catalysts, $\text{m}\cdot\text{s}^{-2}$
$C_d$	drag coefficient
$C_D$	drag coefficient in EMMS model
$C_p$	mixture specific heat at constant pressure, $\text{J}\cdot\text{mol}^{-1}\cdot\text{K}^{-1}$
$C_{p,i}$	specific heat of species $i$ , $\text{J}\cdot\text{kg}^{-1}\cdot\text{K}^{-1}$
$C_v$	specific heat of particle, $\text{J}\cdot\text{kg}^{-1}\cdot\text{K}^{-1}$
D	drag force, $\text{kg}\cdot\text{m}^{-3}\cdot\text{s}^{-1}$
$D$	turbulent mass diffusivity, $\text{m}^2\cdot\text{s}^{-1}$
$D_1$	drag force in Wen-Yu model, $\text{kg}\cdot\text{m}^{-3}\cdot\text{s}^{-1}$
$D_2$	drag force in Gidaspow model, $\text{kg}\cdot\text{m}^{-3}\cdot\text{s}^{-1}$
$d_p$	individual particle diameter, m
$d_{sm}$	Sauter mean diameter, m
f	particle probability distribution function
F	rate of momentum exchange per unit volume, $\text{N}\cdot\text{m}^{-3}\cdot\text{s}^{-1}$
F(t)	cumulative distribution function
g	gravitational acceleration, $\text{m}\cdot\text{s}^{-2}$
$G_s$	solids mass flux, $\text{kg}\cdot\text{m}^{-2}\cdot\text{s}^{-1}$
$h_f$	fluid enthalpy or mixture enthalpy, $\text{J}\cdot\text{mol}^{-1}$
$h_{f,i}$	enthalpy of gas-phase species, $\text{J}\cdot\text{mol}^{-1}$
$h_p$	particle enthalpy, $\text{J}\cdot\text{mol}^{-1}$
$H_D$	heterogeneity index
i	gas-phase species
$N_s$	summation of all gas species
P	gas pressure, Pa
$P_s$	constant, Pa
q	fluid heat flux, $\text{J}\cdot\text{m}^{-2}$
$Q'$	energy source per volume, $\text{J}\cdot\text{m}^{-3}$
R	universal gas constant, $\text{J}\cdot\text{mol}^{-1}\cdot\text{K}^{-1}$
Re	Reynolds number
$Re_p$	particle Reynolds number
Sc	Schmidt number
$S_h$	conservative energy exchange from the particle phase to the fluid phase, $\text{J}\cdot\text{m}^{-3}$
$T_f$	fluid temperature, K
$T_p$	particle temperature, K
$u_f$	gas velocity, $\text{m}\cdot\text{s}^{-1}$
$U_g$	superficial gas velocity, $\text{m}\cdot\text{s}^{-1}$
$u_p$	particle velocity, $\text{m}\cdot\text{s}^{-1}$
$V_p$	particle volume, $\text{m}^3$
$Y_{fi}$	total fluid phase properties from the mass fractions

### Greek letters

$\mu_f$	gas viscosity, $\text{kg}\cdot\text{m}^{-1}\cdot\text{s}^{-1}$
$\rho_f$	fluid density, $\text{kg}\cdot\text{m}^{-3}$
$\rho_g$	gas density, $\text{kg}\cdot\text{m}^{-3}$
$\rho_p$	particle density, $\text{kg}\cdot\text{m}^{-3}$
$\tau_p$	particle normal stress, $\text{N}\cdot\text{m}^{-2}$
$\theta_g$	gas volume fraction
$\theta_p$	particle volume fraction
$\theta_{cp}$	particle-phase volume fraction at close packing
$\beta$	drag force in EMMS model, $\text{kg}\cdot\text{m}^{-3}\cdot\text{s}^{-1}$
$\beta$	constant number, 2–5
$\mu$	viscosity, $\text{Pa}\cdot\text{s}^{-1}$
$\Phi$	energy source per volume, $\text{J}\cdot\text{m}^{-3}$
$\Phi(C_C)$	decay function of the catalyst
$\lambda_f$	fluid thermal conductivity, $\text{W}\cdot\text{m}^{-1}\cdot\text{K}^{-1}$
$Pr_t$	Prandtl number
$\dot{q}_D$	enthalpy diffusion, $\text{J}\cdot\text{mol}^{-1}\cdot\text{s}^{-1}$
$Nu_{f,p}$	Nusselt number

### Acknowledgement

The authors acknowledge the support by the National Natural Science Foundation of China (Grant Nos. 91534204 and 21622609).

### References

- [1] D. Bai, E. Shibuya, Y. Masuda, N. Nakagawa, K. Kato, Flow structure in a fast fluidized bed, *Chem. Eng. Sci.* 51 (1996) 957–966.
- [2] B. Chalermstinsuwan, Y. Prajongkan, P. Piumsomboon, C.F.D. Three-dimensional, Simulation of the system inlet and outlet boundary condition effects inside a high solid particle flux circulating fluidized bed riser, *Powder Technol.* 245 (2013) 80–93.
- [3] T. McKeen, T. Pugsley, Simulation and experimental validation of a freely bubbling bed of FCC catalyst, *Powder Technol.* 129 (2003) 139–152.
- [4] D. Gidaspow, J. Jung, R.K. Singh, Hydrodynamics of fluidization using kinetic theory: an emerging paradigm: 2002 Flour-Daniel lecture, *Powder Technol.* 148 (2004) 123–141.
- [5] H.P. Zhu, Z.Y. Zhou, R.Y. Yang, A.B. Yu, Discrete particle simulation of particulate systems: theoretical developments, *Chem. Eng. Sci.* 62 (2007) 3378–3396.
- [6] C. Chen, J. Werther, S. Heinrich, H.Y. Qi, E.U. Hartge, CPFD simulation of circulating fluidized bed risers, *Powder Technol.* 235 (2013) 238–247.
- [7] X. Shi, R. Sun, X. Lan, F. Liu, Y. Zhang, J. Gao, CPFD simulation of solids residence time and back-mixing in CFB risers, *Powder Technol.* 271 (2015) 16–25.
- [8] Y. Makkawi, P. Wright, R. Ocone, The effect of friction and inter-particle cohesive forces on the hydrodynamics of gas-solid flow: a comparative analysis of theoretical predictions and experiments, *Powder Technol.* 163 (2006) 69–79.
- [9] J. Gao, X. Lan, Y. Fan, J. Chang, G. Wang, C. Lu, C. Xu, CFD modeling and validation of the turbulent fluidized bed of FCC particles, *AIChE J.* 55 (2009) 1680–1694.
- [10] O. Molerus, Interpretation of Geldart type A, B, C and D powders by taking into account interparticle forces, *Powder Technol.* 33 (1982) 81–87.
- [11] M.J. Rhodes, X.S. Wang, M. Nguyen, P. Stewart, K. Liffman, Onset of cohesive behavior in gas fluidized beds: a numerical study using DEM simulation, *Chem. Eng. Sci.* 56 (2001) 4433–4438.
- [12] H.P. Zhu, Z.Y. Zhou, R.Y. Yang, A.B. Yu, Discrete particle simulation of particulate systems: a review of major applications and findings, *Chem. Eng. Sci.* 63 (2008) 5728–5770.
- [13] N.G. Deen, M.V.S. Annaland, M.A.V.D. Hoef, J.A.M. Kuipers, Review of discrete particle modeling of fluidized beds, *Chem. Eng. Sci.* 62 (2007) 28–44.
- [14] D.M. Snider, Three fundamental granular flow experiments and CPFD predictions, *Powder Technol.* 176 (2007) 36–46.
- [15] D.M. Snider, An incompressible three-dimensional multiphase particle-in-cell model for dense particle flows, *J. Comput. Phys.* 170 (2001) 523–549.
- [16] F. Li, F. Song, S. Benyahia, W. Wang, J. Li, MP-PIC simulation of CFB riser with EMMS-based drag model, *Chem. Eng. Sci.* 82 (2012) 104–113.
- [17] S. Karimipour, T. Pugsley, Application of the particle in cell approach for the simulation of bubbling fluidized beds of Geldart A particles, *Powder Technol.* 220 (2012) 63–69.
- [18] D.M. Snider, S. Banerjee, Heterogeneous gas chemistry in the CPFD Eulerian-Lagrangian numerical scheme (ozone decomposition), *Powder Technol.* 199 (2010) 100–106.
- [19] D.M. Snider, S.M. Clark, P.J. O'Rourke, Eulerian-Lagrangian method for three-dimensional thermal reacting flow with application to coal gasifiers, *Chem. Eng. Sci.* 66 (2011) 85–1295.
- [20] C. Wang, High-density Gas-Solids Circulating Fluidized Bed Riser and Downer Reactors, Dissertation The University of Western Ontario, Canada, 2013.
- [21] P.J. O'Rourke, Collective drop effects on vaporizing liquid sprays[R], Los Alamos National Lab., NM (USA), 1981 321–325.
- [22] T. Li, C. Guenther, MFX-DEM simulations of change of volumetric flow in fluidized beds due to chemical reactions, *Powder Technol.* 220 (2011) 70–78.
- [23] W. Li, K. Yu, B. Liu, X. Yuan, Computational fluid dynamics simulation of hydrodynamics and chemical reaction in a CFB downer, *Powder Technol.* 269 (2015) 425–436.
- [24] L. Kong, J. Zhu, C. Zhang, Catalytic ozone decomposition in a gas-solids circulating fluidized-bed riser, *Chem. Eng. Technol.* 37 (2014) 435–444.
- [25] C. Chen, J. Werther, S. Heinrich, H.Y. Qi, E.U. Hartge, CPFD simulation of circulating fluidized bed risers, *Powder Technol.* 235 (2013) 238–247.
- [26] W. Wang, B. Lu, W. Dong, J. Li, Multi-scale CFD simulation of operating diagram for gas-solid risers, *Can. J. Chem. Eng.* 86 (2008) 448–457.
- [27] B. Lu, W. Wang, J. Li, Searching for a mesh-independent sub-grid model for CFD simulation of gas-solid riser flows, *Chem. Eng. Sci.* 64 (2009) 3437–3447.
- [28] N. Yang, W. Wang, W. Ge, J. Li, CFD simulation of concurrent-up gas-solid flow in circulating fluidized beds with structure-dependent drag coefficient, *Chem. Eng. J.* 96 (2003) 71–80.
- [29] M.T. Shah, R.P. Utikar, V.K. Pareek, M.O. Tade, G.M. Evans, Effect of closure models on Eulerian-Eulerian gas-solid flow predictions in riser, *Powder Technol.* 269 (2015) 247–258.
- [30] T. Li, C. Guenther, A CFD study of gas-solid jet in a CFB riser flow, *AIChE J.* 58 (2012) 756–769.
- [31] K. Agrawal, P.N. Loezos, M. Syamlal, S. Sundaresan, The role of meso-scale structures in rapid gas-solid flows, *J. Fluid Mech.* 445 (2001) 151–185.
- [32] X. Shi, Y. Wu, X. Lan, F. Liu, J. Gao, Effects of the riser exit geometries on the hydrodynamics and solids back-mixing in CFB risers: 3D simulation using CPFD approach, *Powder Technol.* 284 (2015) 130–142.

- [33] S.Z. And, F. Taghipour, CFD modeling of the hydrodynamics and reaction kinetics of FCC fluidized-bed reactors, *Ind. Eng. Chem. Res.* 44 (2005) 9818–9827.
- [34] X. Lan, C. Xu, G. Wang, L. Wu, J. Gao, CFD modeling of gas-solid flow and cracking reaction in two-stage riser FCC reactors, *Chem. Eng. Sci.* 64 (2009) 3847–3858.
- [35] J. Gao, C. Xu, S. Lin, G. Yang, Y. Guo, Simulations of gas-liquid-solid 3-phase flow and reaction in FCC riser reactors, *AIChE J.* 47 (2001) 677–692.
- [36] J. Gao, C. Xu, S. Lin, G. Yang, Y. Guo, Advanced model for turbulent gas-solid flow and reaction in FCC riser reactors, *AIChE J.* 45 (1999) 1095–1113.